RESEARCH PROPOSAL

Image-space wave-equation tomography for anisotropic parameters

Yunyue (Elita) Li

11:00, Wednesday, June 2, 2010

ABSTRACT

Anisotropic models are widely needed by many anisotropic migration and interpretation schemes to obtain clearer image and thereby better understanding of the complex subsurface. However, anisotropic model building is a notoriously challenging problem because of its non-linearity and the existence of trade-off among the anisotropic parameters. I propose an approach to build the anisotropic model using Wave-Equation Tomography (WETom) with two major features: first, WETom will be performed in the image-space, and provide a direct link between the model perturbation and the image perturbation; and second, WETom will include various regularization schemes to incorporate as much prior information as possible. Previous implementation of WETom operator builds the cornerstone of the proposed process, and the preliminary results on simple 2-D examples demonstrate its feasibility. Ultimately, I aim to utilize all the information available – surface seismic data and the borehole data; measure of image in terms of both focusness and moveout – to build a consistent, reliable anisotropic model, and produce a well-focused image at the same time.

PROBLEM STATEMENT

Since first reported in exploration seismology in the 1930s (McCollum and Snell, 1932), the importance of anisotropy has been continuously increased in seismic imaging and exploration. This is partially due to acquisition with increasingly longer offsets and exploration in areas with strong geological deformation. In these circumstances, accurate understanding of the anisotropic behavior of wave propagation is crucial to the overall success of an imaging project. Seismic data processing that ignores anisotropy leads to kinematic errors, which become worse when imaging steep reflectors such as salt flanks or steep faults. This could cause severe consequences for potential drilling or production. Therefore, numerous anisotropic migration and processing schemes have been developed during the past decade (Shan, 2009; Fletcher et al., 2009; Zhang and Zhang, 2009; Fei and Liner, 2008), but their application requires knowledge of the anisotropic velocity model. Obviously, it is far more complicated to recover several independent elastic coefficients needed to construct the anisotropic velocity function than to perform conventional velocity analysis for isotropic media.

There are two main difficulties that cause the estimation of anisotropic model unreliable: first, current anisotropic model-building schemes are mostly ray-based approach, measuring the non-hyperbolic moveout along the traveltime curve, which are prone to errors and unrealistic results when multi-pathing exists in areas of complex overburden; and second, the trade-off among the anisotropic parameters cannot be resolved by surface reflection data only due to the lack of vertical information. Recently, researches on anisotropic tomography near wells have been presented (Bakulin

et al., 2009). However, these results are highly localized within the surrounding area of the well, and therefore have little information for the areas farther away from the wells. Therefore, a new scheme that yields reliable anisotropic velocity models in the seismic scale is needed.

PROPOSED SOLUTION

Here, I propose a project that aims to produce a reliable anisotropic velocity model for various migration and processing schemes by incorporating both surface seismic data and borehole information in an image-space wave-equation tomography fashion. As mentioned in previous sections, the data-space ray-based approach is vulnerable when the data are contaminated with noise and the geological environments are complex, while image-space wave-equation migration velocity analysis approach is stable and efficient because it works on much cleaner images and can be implemented in a target-oriented fashion. Therefore, I propose to design a machinery – anisotropic wave-equation tomography (AWETom) operator – that provides a direct mapping between the change in the image space and the change in the anisotropic model. The change in the image can be measured either by computing the focusness (at zero-subsurface offset) of the subsurface offset common image gathers (SODCIGs) or by computing the coherence of angle domain common image gathers (ADCIGs). The back-projected changes in the anisotropic model space will be used as gradient directions to conduct a line-search in optimization schemes. The application of the image-space wave-equation tomography is very computational intensive. Therefore, I will apply a target-oriented tomography strategy and a phase-encoding method to reduce the computational cost.

Clearly, inversion for anisotropic parameters is highly non-linear and underdetermined. Therefore, proper model space regularization is necessary to better constrain the inversion process. I propose to apply a regularizer which is a linear combination of the steering filter and the smoothing operator aligned with sea bottom slope to characterize the anisotropy both due to the mineral alignment during deposition and due to the overburden compaction after deformation. Furthermore, observations show that anisotropic parameters generally have similar structures. Therefore, a cross-gradient regularization (Gallardo and Meju, 2004) among the model parameters can be another useful constrain.

As discussed before, use of single type of data – surface seismic only or borehole data only – will either introduce ambiguities among the anisotropic parameters or fail to predict the anisotropic property away from the well. Therefore, I propose to utilize both information, and thereby includes input of different resolution and different sensitivity in different directions. I hope to incorporate all the available information to resolve a reliable anisotropic velocity model.

PARAMETERIZATION

In the VTI medium, Thomsen parameters ϵ and δ are commonly used to characterize the anisotropic property. These two parameters define the relationships between the vertical velocity (V_V), the horizontal velocity (V_H), and the NMO velocity (V_N) as follows:

$$V_H^2 = V_V^2(1+2\epsilon) \quad (1)$$

$$V_N^2 = V_V^2(1+2\delta) \quad (2)$$

In the practice of the surface seismic exploration, it is impossible to estimate the vertical velocity because depth of the reflectors is unknown, and there is no vertical offset information in the data. However, if there is long enough offset in the in-line and cross-line direction, it is possible to resolve the horizontal velocity and the NMO velocity. Therefore, the anellipticity parameter η is used to link directly between V_N and V_H:

$$V_H^2 = V_N^2(1+2\eta) \quad (3)$$

where η is defined by the Thomsen parameters as follows:

$$\eta = \frac{\epsilon - \delta}{(1+2\delta)} \quad (4)$$

In the current implementation, to reduce the number of the parameters, thereby the null space of the inversion, I make an arbitrary assumption that $\delta = 0$. Hence, there are only two independent parameters left:

$$\eta = \epsilon \quad (5)$$

$$V_N = V_V \quad (6)$$

Therefore, V_N and η are the parameters to be estimated during the inversion.

The assumption of $\delta = 0$ is apparently non-physical in certain geological environments. However, δ usually can be obtained from the borehole data - welllogs and checkshots. Therefore, it is reasonable to assume δ is known from other sources, and only invert for V_N and η as discussed above.

When TTI media is considered, another two parameters α and β are introduced into the model to characterize the tilted angle in the 3-D space. This adds another two levels of complexity. Fortunately, the tilted angle α and β can be estimated at each non-linear iteration from the current image, and used directly as known information. Therefore, V_N and η are still the only parameters to be estimated by the inversion process.

THEORY

Anisotropic wave-equation tomography operator

Anisotropic WETom is a non-linear inversion process that aims to find the anisotropic model that minimizes the residual field $\Delta\mathbf{I}$ in the image space. The residual image is derived from the background image $\mathbf{I}$, which is computed with current background model. In general, the residual image is defined as (Biondi, 2008)

$$\Delta\mathbf{I} = \mathbf{I} - \mathbf{F}(\mathbf{I}), \tag{7}$$

where $\mathbf{F}$ is a focusing operator acting on the background image.

In the least-squares sense, the tomographic objective function can be written as follows:

$$J = \frac{1}{2}||\Delta\mathbf{I}||_2 = \frac{1}{2}||\mathbf{I} - \mathbf{F}(\mathbf{I})||_2. \tag{8}$$

To perform the WETom for anisotropic parameters, I first need to extend the tomographic operator from the isotropic medium (Shen, 2004; Sava, 2004; Guerra et al., 2009) to the anisotropic medium. I define the image-space wave-equation tomographic operator $\mathbf{T}$ for anisotropic parameters as follows:

$$\begin{aligned} \mathbf{T} &= \left.\frac{\partial \mathbf{I}}{\partial \mathbf{m}}\right|_{\mathbf{m}=\widehat{\mathbf{m}}} \\ &= \left.\frac{\partial \mathbf{I}}{\partial \mathbf{s}}\right|_{\mathbf{s}=\widehat{\mathbf{s}}} + \left.\frac{\partial \mathbf{I}}{\partial \eta}\right|_{\eta=\widehat{\eta}}, \end{aligned} \tag{9}$$

where $\mathbf{m}$ is the anisotropy model, which in this case includes vertical slowness $\mathbf{s}$ and anellipticity parameter η; $\widehat{\mathbf{m}}$ is the background anisotropy model, consisting of the background slowness $\widehat{\mathbf{s}}$ and background anellipticity $\widehat{\eta}$; $\mathbf{I}$ is the image. This WETom operator $\mathbf{T}$ is a linear operator that relates the model perturbation $\Delta\mathbf{m}$ to the image perturbation $\Delta\mathbf{I}$ as follows:

$$\Delta\mathbf{I} = \mathbf{T}\Delta\mathbf{m}. \tag{10}$$

In the current implementation, I evaluate the anisotropic tomographic operator in the shot-profile domain.

Both source and receiver wavefields are downward continued in the shot-profile domain using the one-way wave equations (Claerbout, 1971):

$$\begin{cases} \left(\frac{\partial}{\partial z} + i\Lambda\right) D(\mathbf{x}, \mathbf{x}_s) = 0 \\ D(x, y, z = 0, \mathbf{x}_s) = f_s \delta(\mathbf{x} - \mathbf{x}_s) \end{cases}, \tag{11}$$

and

$$\begin{cases} \left(\frac{\partial}{\partial z} - i\Lambda\right) U(\mathbf{x}, \mathbf{x}_s) = 0 \\ U(x, y, z = 0, \mathbf{x}_s) = Q(x, y, z = 0, \mathbf{x}_s) \end{cases}, \tag{12}$$

where $D(\mathbf{x}, \mathbf{x}_s)$ is the source wavefield at the image point $\mathbf{x} = (x, y, z)$ with the source located at $\mathbf{x}_s = (x_s, y_s, 0)$; $U(\mathbf{x}, \mathbf{x}_s)$ is the receiver wavefield at the image point $\mathbf{x}$ with the source located at $\mathbf{x}_s$; f_s is the source signature, and $f_s\delta(\mathbf{x} - \mathbf{x}_s)$ defines the point source function at $\mathbf{x_s}$, which serves as the boundary condition of equation 11; $Q(x, y, z = 0, \mathbf{x}_s)$ is the recorded shot gather at $\mathbf{x}_s$, which serves as the boundary condition of Equation 12. Operator Λ is the dispersion relationship for anisotropic wave propogation (Shan, 2009):

$$\Lambda = \omega s(\mathbf{x}) \sqrt{1 - \frac{|\mathbf{k}|^2}{\omega^2 s^2(\mathbf{x}) - 2\eta(\mathbf{x})|\mathbf{k}|^2}}, \tag{13}$$

where ω is the angular frequency, $s(\mathbf{x})$ is the slowness at $\mathbf{x}$, $\eta(\mathbf{x})$ is the anellipticity at $\mathbf{x}$; $\mathbf{k} = (k_x, k_y)$ is the spatial wavenumber vector. Dispersion relationship 13 can be approximated with a rational function by Taylor series and Padé expansion analysis:

$$\Lambda = \omega s(\mathbf{x}) \big(1 - \frac{a|\mathbf{k}|^2}{\omega^2 s^2(\mathbf{x}) - b|\mathbf{k}|^2}\big), \tag{14}$$

where, to the second order, $a = 0.5, b = 2\eta + 0.25$. Using binomial expansion, Equation 14 can be further expanded to polynomials:

$$\Lambda = \omega s(\mathbf{x}) - \frac{a}{\omega s^2(\mathbf{x})}|\mathbf{k}|^2 - \frac{3ab}{\omega^3 s^4(\mathbf{x})}|\mathbf{k}|^4. \tag{15}$$

The background image is computed by applying the cross-correlation imaging condition:

$$I(\mathbf{x}, \mathbf{h}) = \sum_{\mathbf{x}_s} \sum_{\omega} \overline{D(\mathbf{x} - \mathbf{h}, \mathbf{x}_s)} U(\mathbf{x} + \mathbf{h}, \mathbf{x}_s), \tag{16}$$

where the bar stands for the complex conjugate, and $\mathbf{h} = (h_x, h_y, h_z)$ is the subsurface half-offset.

Under the Born approximation, a perturbation in the model parameters causes a first-order perturbation in the wavefields. Consequently, the resulting image perturbation reads:

$$\begin{aligned} \Delta I(\mathbf{x}, \mathbf{h}) \;=\; & \sum_{\mathbf{x}_s} \sum_{\omega} \Big(\overline{\Delta D(\mathbf{x} - \mathbf{h}, \mathbf{x}_s)} \widehat{U}(\mathbf{x} + \mathbf{h}, \mathbf{x}_s) + \\ & \overline{\widehat{D}(\mathbf{x} - \mathbf{h}, \mathbf{x}_s)} \Delta U(\mathbf{x} + \mathbf{h}, \mathbf{x}_s) \Big), \end{aligned} \tag{17}$$

where $\widehat{D}(\mathbf{x}-\mathbf{h}, \mathbf{x}_s)$ and $\widehat{U}(\mathbf{x}+\mathbf{h}, \mathbf{x}_s)$ are the background source and receiver wavefields computed with the background model $\widehat{m}(\mathbf{x})$, $\Delta D(\mathbf{x} - \mathbf{h}, \mathbf{x}_s)$ and $\Delta U(\mathbf{x} + \mathbf{h}, \mathbf{x}_s)$ are the perturbed source wavefield and perturbed receiver wavefield, respectively, which result from the model perturbation $\Delta m(\mathbf{x})$.

To evaluate the adjoint tomographic operator $\mathbf{T}^*$, which backprojects the image perturbation into the model space, first compute the wavefield perturbation from the image perturbation using the adjoint imaging condition:

$$\begin{aligned} \Delta D(\mathbf{x},\mathbf{x}_s) &= \sum_{\mathbf{h}} \Delta I(\mathbf{x},\mathbf{h}) \widehat{U}(\mathbf{x}+\mathbf{h},\mathbf{x}_s) \\ \Delta U(\mathbf{x},\mathbf{x}_s) &= \sum_{\mathbf{h}} \Delta I(\mathbf{x},\mathbf{h}) \widehat{D}(\mathbf{x}-\mathbf{h},\mathbf{x}_s). \end{aligned} \tag{18}$$

The perturbed source and receiver wavefields satisfy the following one-way wave equations, linearized with respect to slowness and η:

$$\begin{cases} \left(\frac{\partial}{\partial z} + i\Lambda\right) \Delta D(\mathbf{x},\mathbf{x}_s) = \left(-i\frac{\partial \Lambda}{\partial \mathbf{m}} \widehat{D}(\mathbf{x},\mathbf{x}_s)\right) \Delta \mathbf{m}^*(\mathbf{x}) \\ \Delta D(x,y,z=0,\mathbf{x}_s) = 0 \end{cases}, \tag{19}$$

and

$$\begin{cases} \left(\frac{\partial}{\partial z} - i\Lambda\right) \Delta U(\mathbf{x},\mathbf{x}_s) = \left(-i\frac{\partial \Lambda}{\partial \mathbf{m}} \widehat{U}(\mathbf{x},\mathbf{x}_s)\right) \Delta \mathbf{m}^*(\mathbf{x}) \\ \Delta U(x,y,z=0,\mathbf{x}_s) = 0 \end{cases}, \tag{20}$$

where $\mathbf{m}$ is the row vector $[\mathbf{s}\ \eta]$, and $\mathbf{m}^*$ is the transpose of $\mathbf{m}$.

When solving the optimization problem, I obtain the image perturbation by migrating the data with the current background model and performing a focusing operation (Equation 7). Then the perturbed image is convolved with the background wavefields to get the perturbed wavefields (Equation 18). The scattered wavefields are computed by applying the adjoint of the one-way wave-equations 19 and 20. Finally, the model space gradient is obtained by cross-correlating the upward propagated scattered wavefields with the modified background wavefields (terms in the parentheses on the right-hand sides of Equations 19 and 20).

Figure 1 shows the work flow for the image-space wave-equation tomography. Currently, I define the focusing operator by the Differential Semblance Optimization (DSO) (Shen, 2004) method for its simplicity. However, DSO is not the best focusing operator for its strong artifacts in the gradient and its lack of ability to resolve the ambiguity between the illumination artifacts and the velocity errors. A possible substitute is the wave-equation migration velocity analysis (WEMVA) objective function (Sava and Biondi, 2004). The challenge for this substitution is to generalize WEMVA to anisotropic media; this will be my future research topic.

Prestack exploding-reflector modeling

The idea of prestack exploding-reflector modeling (Biondi, 2006) is to synthesize the data using one isolated SODCIG as an initial condition. In this case, the synthesized source and receiver wavefields are computed as follows:

$$\begin{cases} \left(\frac{\partial}{\partial z} - i\Lambda\right) Q_D(\mathbf{x};x_m,y_m) = I_D(\mathbf{x},\mathbf{h};x_m,y_m) \\ Q_D(x,y,z=z_{\max};x_m,y_m) = 0 \end{cases}, \tag{21}$$

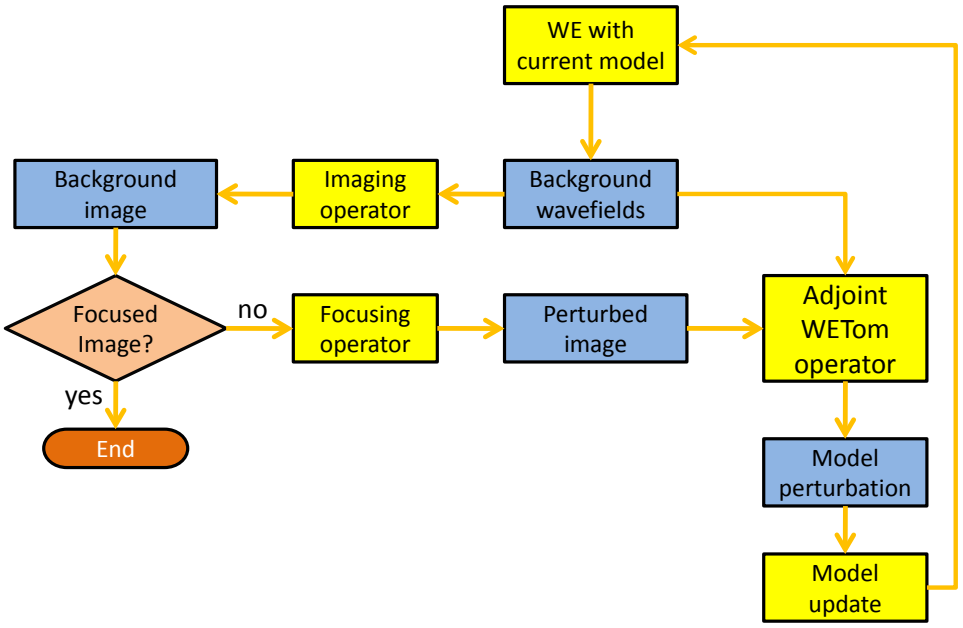

Figure 1: Flowchart of the inversion process. WE stands for Wavefield Extrapolation. Adjoint WETom operator is chained by adjoint imaging operator, adjoint wavefield extrapolation, and adjoint scattering operator.

and

$$\begin{cases} \left(\frac{\partial}{\partial z} - i\Lambda\right) Q_U(\mathbf{x}; x_m, y_m) = I_U(\mathbf{x}, \mathbf{h}; x_m, y_m) \\ Q_U(x, y, z = z_{\max}; x_m, y_m) = 0 \end{cases}, \tag{22}$$

where $I_D(\mathbf{x}, \mathbf{h}; x_m, y_m)$ and $I_U(\mathbf{x}, \mathbf{h}; x_m, y_m)$ are the isolated SODCIGs at the horizontal location (x_m, y_m) for a single reflector. They are acting as the intial conditions for the source and the receiver wavefields, respectively. $Q_D(\mathbf{x}; x_m, y_m)$ and $Q_U(\mathbf{x}; x_m, y_m)$ are the synthesized source and receiver wavefields, respectively. Λ is the square-root operator defined by equation (13).

One benefit of using prestack exploding-reflector modeling is that, the wavefields can be collected at a certain depth level or horizon (which is not necessarily to be the surface of the earth), provided the model above is sufficiently accurate. The collected data $Q_D(x, y, z = z_0; x_m, y_m) = 0$ and $Q_U(x, y, z = z_0; x_m, y_m) = 0$ are so called areal source data and areal receiver data, respectively.

Image-space phase-encoded wavefields

In practice, the migrated image volume can be very large and contains many reflectors. Prestack exploding-reflector modeling can be thereby very computational expensive, and may result in even larger dataset than the original one. Guerra and Biondi

(2008) demonstrate that random phase encoding can reduce the cost by modeling several reflectors and several SODCIGs simultaneously and attenuate the cross talk at the same time.

The randomly encoded areal source and receiver wavefields can be computed as follows:

$$\begin{cases} \left(\frac{\partial}{\partial z} - i\Lambda\right) \widetilde{Q}_D(\mathbf{x}, \mathbf{p}_m, \omega) = \widetilde{I}_D(\mathbf{x}, \mathbf{h}, \mathbf{p}_m, \omega) \\ \widetilde{Q}_D(x, y, z = z_{\max}, \mathbf{p}_m, \omega) = 0 \end{cases}, \tag{23}$$

and

$$\begin{cases} \left(\frac{\partial}{\partial z} - i\Lambda\right) \widetilde{Q}_U(\mathbf{x}, \mathbf{p}_m, \omega) = \widetilde{I}_U(\mathbf{x}, \mathbf{h}, \mathbf{p}_m, \omega) \\ \widetilde{Q}_U(x, y, z = z_{\max}, \mathbf{p}_m, \omega) = 0 \end{cases}, \tag{24}$$

where $\widetilde{I}_D(\mathbf{x}, \mathbf{h}, \mathbf{p}_m, \omega)$ and $\widetilde{I}_U(\mathbf{x}, \mathbf{h}, \mathbf{p}_m, \omega)$ are the encoded SODCIGs. They are defined as:

$$\begin{array}{l} \widetilde{I}_D(\mathbf{x}, \mathbf{h}, \mathbf{p}_m, \omega) = \sum_{x_m, y_m} I_D(\mathbf{x}, \mathbf{h}, x_m, y_m)\beta, \\ \widetilde{I}_U(\mathbf{x}, \mathbf{h}, \mathbf{p}_m, \omega) = \sum_{x_m, y_m} I_U(\mathbf{x}, \mathbf{h}, x_m, y_m)\beta, \end{array} \tag{25}$$

where $\beta = e^{i\gamma(\mathbf{x}, x_m, y_m, \mathbf{p}_m, \omega)}$ is chosen to be the random phase-encoding function, with $\gamma(\mathbf{x}, x_m, y_m, \mathbf{p}_m, \omega)$ being a uniformly distributed random sequence in $\mathbf{x}$, x_m, y_m and ω; the variable $\mathbf{p}_m$ is the index of different realizations of the random sequence. Similarly, the encoded areal source data $\widetilde{I}_D(\mathbf{x}, \mathbf{h}, \mathbf{p}_m, \omega)$ and the encoded areal receiver data $\widetilde{I}_D(\mathbf{x}, \mathbf{h}, \mathbf{p}_m, \omega)$ can be collected at any depth.

During the tomography, the synthesized data are downward continued using one-way wave-equation described in the previous section. The computation for background image and perturbed image for single realization remains the same; the final images are obtained by summing over all the realizations $\mathbf{p}_m$.

Model-space regularization

As stated previously, anisotropic model building is highly non-linear and underdetermined. Therefore, proper model-space regularization should be designed to incorporate as much prior information into the inversion as possible.

In general, there are two main origins of anisotropy for the transverse isotropic media: first, the mineral alignment in the rock during the deposition, such as preferred orientation (texture) of clay platelets (Kaarsberg, 1959). This kind of anisotropy tends to follow the geological structure, and can be represented by steering filters (Clapp, 2000); second, the compaction from the overburden after the deformation. This kind of anisotropy tends to extend parallel to constant burial depth lines (for example in marine envirionment parallel to the seafloor), and can be represented by a smoothing operator in that perticular direction. Therefore, I propose to impose a

linear combination of these two filters, weights for each filter determined by the depth of the buried section. To be explicit, the deeper the section is, the more weight goes to the horizontal smoothing operator.

Observations show that anisotropic parameters generally have similar structures, as demonstrated by Figure 11, 12 and 13. Therefore, a cross-gradient regularizer can be applied among the anisotropic parameters to enhance the similar structures and penalize the abrupt difference.

It can be challenging to determine which regularizor to use and the relative weights of these regularizors. I will experiment on these different regularization schemes in my later research to examine the effect of them in different geological settings.

WORK COMPLETED

Numerical test of the anisotropic WETom operator

To test the anisotropic WETom operator, we run the forward and adjoint WETom operator on a 2-D model. Figure 2 shows the background isotropic model, with one reflector in velocity and no anisotropy. The data are modeled with 4000m maximum offset, 8m receiver spacing, 80m source spacing and 41 split-spread shots. We use the two-way acoustic anisotropic modeling code in Madagascar to do the modeling, and the one-way SSF (Tang and Clapp, 2006) extrapolator to do the migration.

Figure 3 shows the model perturbations, with a rectangular slowness anomaly that is 10% lower than the background slowness on the left, and a rectangular anisotropic anomaly on the right. The perturbation in η within the rectangular block is constant ($\Delta\eta = 0.1$). Figure 4 shows the perturbed image at the zero lag of the subsurface offset due to the model perturbations after applying the forward WETom operator. Adjoint WETom operator back-projects the perturbed image into the model space, and outputs the gradient for the model perturbation, as shown in Figure 5.

Comparing Figure 3 and Figure 5, I can see in general that the gradients provide the correct direction and shape of the perturbation to conduct a line search in a given inversion scheme. The strong energy concentrated above the reflector is caused by the curvature in the perturbed image away from zero offset. Notice that the side lobes in η is relatively stronger compared with that in slowness, which shows the higher sensitivity of η for large offsets data.

Preliminary results on 2-D VTI Inversion

From the gradient given by the anisotropic WETom operator in last section, we notice that the perturbations in slowness and η are co-located. This is an intrinsic characteristic of the operator, which may not be geologically realistic. Therefore, we design three tests to examine this effect in the inversion.

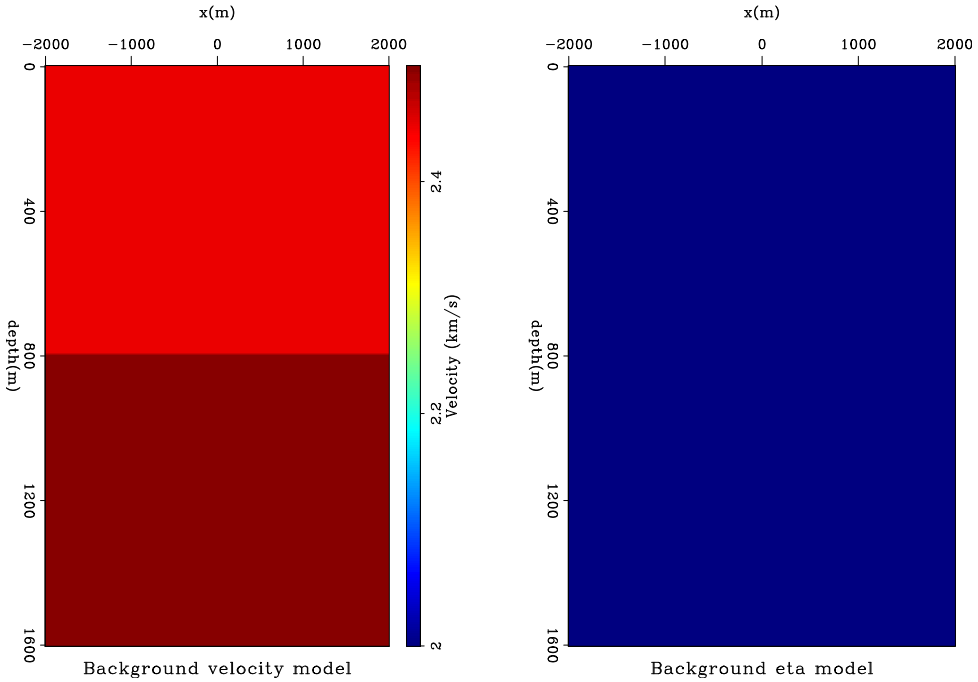

Figure 2: Background isotropic model. Left is the velocity model with one reflector, and right is the η model with constant zero. [**ER**]

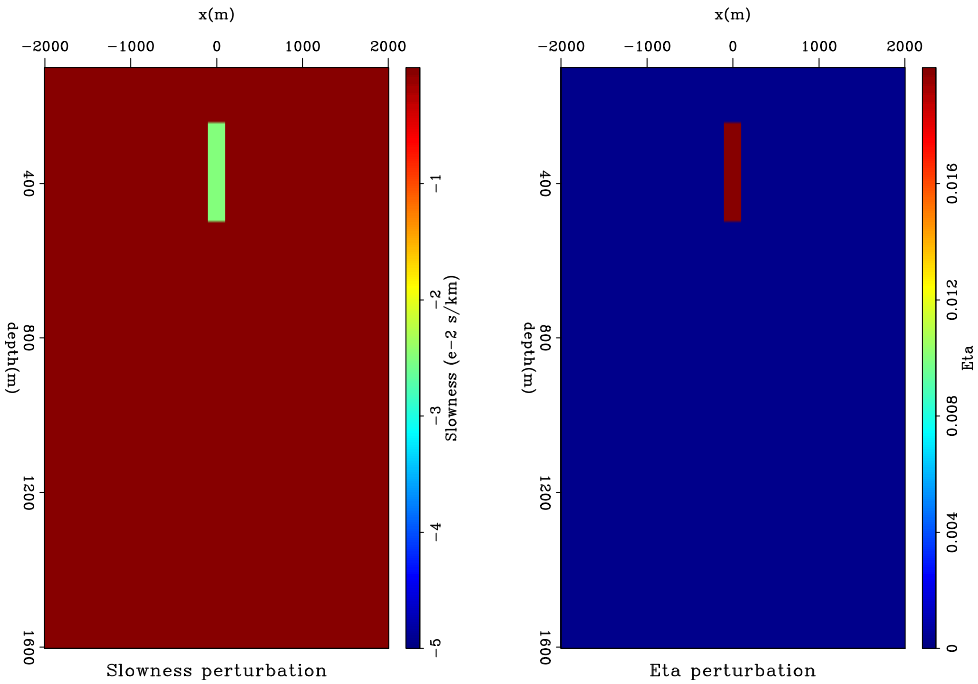

Figure 3: Model perturbations. Left is a rectangular slowness anomaly that is 10% lower than the background slowness , and right is a rectangular anisotropic anomaly with a constant value of $\Delta\eta = 0.1$. [**ER**]

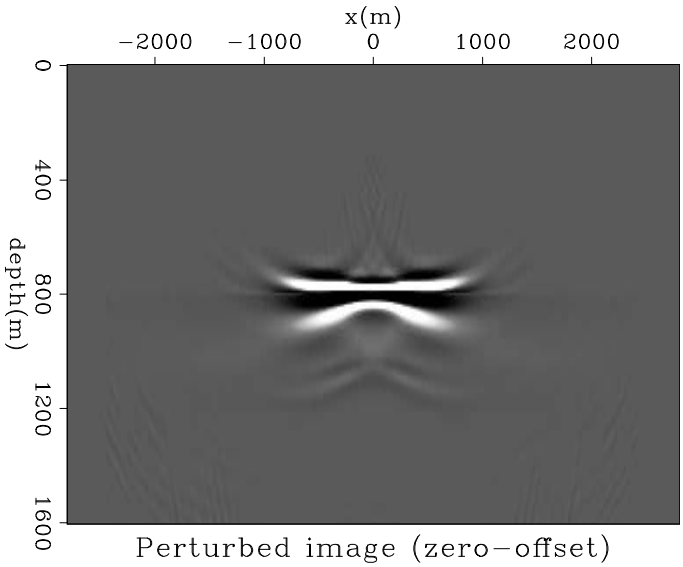

Figure 4: Perturbed image from the forward anisotropic WETom operator. The image is extracted from the zero lag of the subsurface offset. [**ER**]

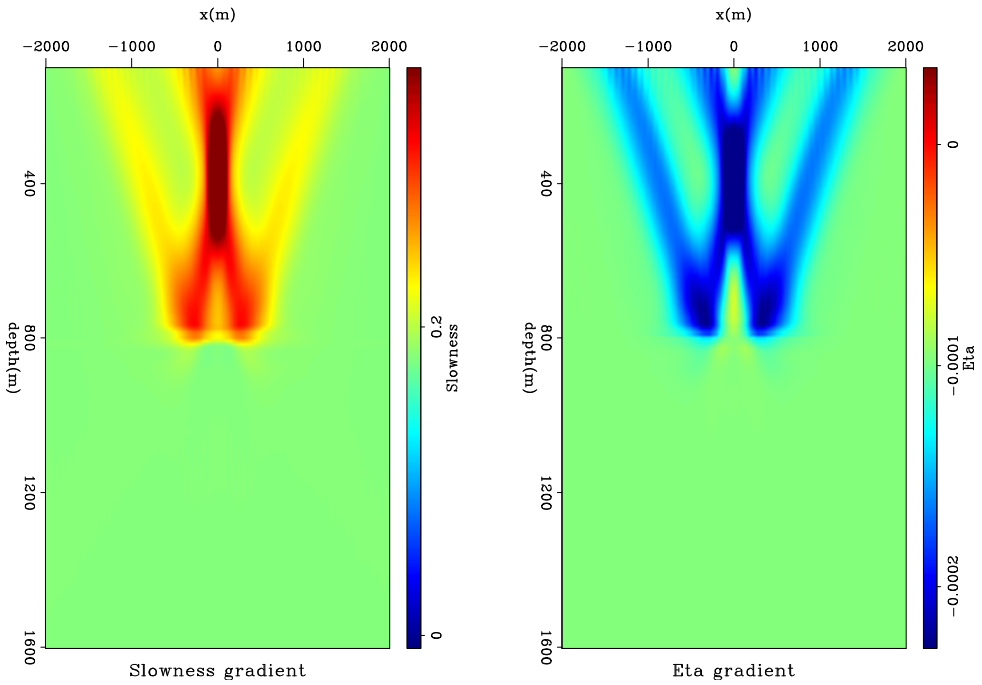

Figure 5: Back-resolved gradient for the model updates. Left is the gradient for slowness, and right is the gradient for η. [**ER**]

In these three tests, we use the same initial model (Figure 6), but data modeled using different true models. In Figure 7 we show the true model perturbations, which have one layer of perturbations in slowness only, in η only, and in both. Figure 8 shows the angle-domain common image gathers (ADCIGs) using the initial model, where ADCIGs are not flat due to the error in the model. Notice the image perturbation is small for the perturbation in η only.

In this realization, we define the focusing operator in the perturbed image (Equation 7) by the Differential Semblance Optimization (DSO) method (Shen, 2004):

$$\mathbf{F}(\mathbf{I}) = (\mathbf{1} - \mathbf{O})\mathbf{I}, \tag{26}$$

where $\mathbf{1}$ is the identity operator and $\mathbf{O}$ is the DSO operator. Therefore, the objective function (Equation 8) becomes:

$$J = \frac{1}{2}||\mathbf{O}\widehat{\mathbf{I}}||^2 = \frac{1}{2}||h\widehat{\mathbf{I}}||^2, \tag{27}$$

where h is the subsurface half-offset. Since the DSO operator is independent of the model parameters, the gradient of J with respect to the model parameters is

$$\nabla J = \left(\frac{\partial \mathbf{I}}{\partial \mathbf{m}}\bigg|_{\mathbf{m}=\widehat{\mathbf{m}}}\right)^* \mathbf{O}^*\mathbf{O}\widehat{\mathbf{I}} = \mathbf{T}^*\mathbf{O}^*\mathbf{O}\widehat{\mathbf{I}}. \tag{28}$$

To minimize the objective function, we specifically use the steepest descent algorithm. To help convergence, we average the gradient at each depth to ensure a layered model and mute the shallow updates to avoid near-surface artifacts.

Figure 9 shows the final model updates after 4 non-linear iterations. The results should be comparable to the model perturbations in Figure 7. In the final updates, we see a consistent over prediction of η. This is because error in η has a very small contribution in the image perturbation, as shown in the middle panel of Figure 8. Figure 10 shows the ADCIGs computed using the updated model. Comparing Figure 7 and Figure 9, Figure 8 with Figure 10, it can be concluded that the inversion successfully identifies the layered perturbation and flattens the ADCIGs. However, the inverted perturbations show up in both parameter spaces, although it is caused by perturbations in a single parameter. Therefore, the ambiguity between the velocity and the anellipticity cannot be resolved simply by the inversion when there are only flat reflectors. I hope that by adding dipping reflectors and thereby increasing the angle coverage of the ray pathes, better definition of the model can be achieved. Also for the case of perturbing both spaces, the over-prediction of velocity perturbation and the under-prediction of η perturbation reconcile with each other and produce flat events in the ADCIGs. Therefore, the inversion process has a big null-space, which requires auxiliary information to further distinguish the difference.

FUTURE WORK

The previous sections have demonstrated that building a reliable anisotropic velocity model using image-space wave-equation methods is possible. The actual work of

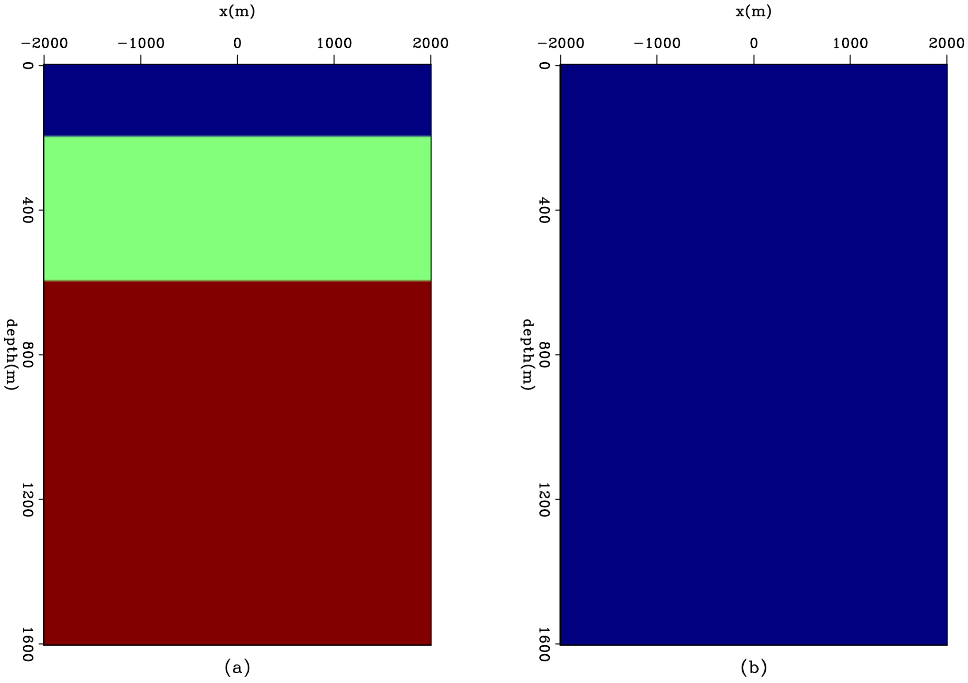

Figure 6: Initial model for inversion. Panel (a) is the initial velocity model with three layers; Panel (b) is the initial η model with constant value of zero. [**ER**]

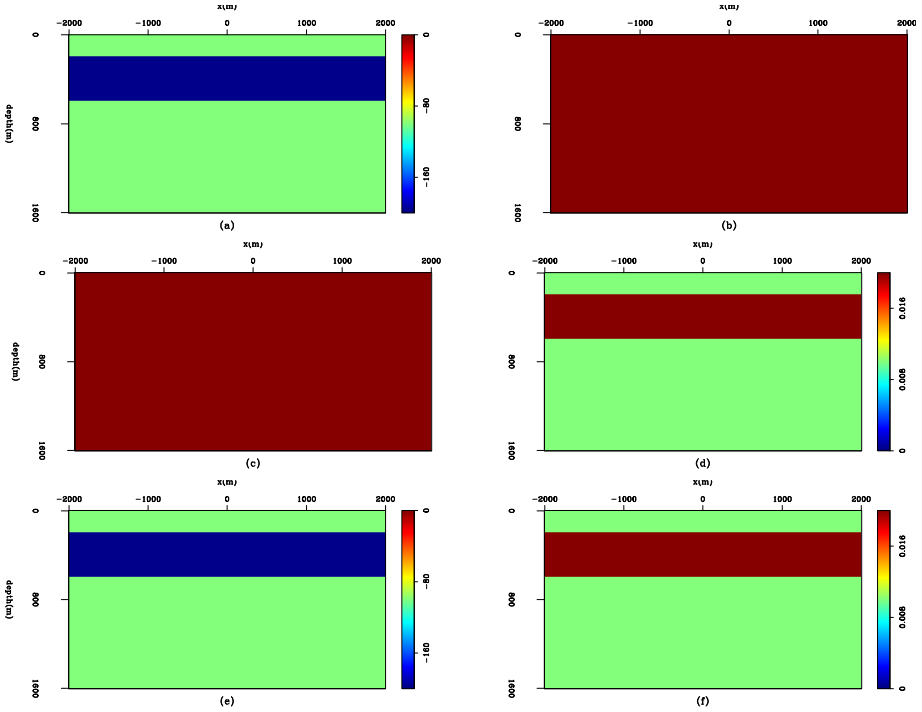

Figure 7: True model perturbation in three test cases. Panel (a) and (b): Perturbation in velocity only; Panel (c) and Panel (d): Perturbation in η only; Panel (e) and Panel (f): Perturbations in both. [**ER**]

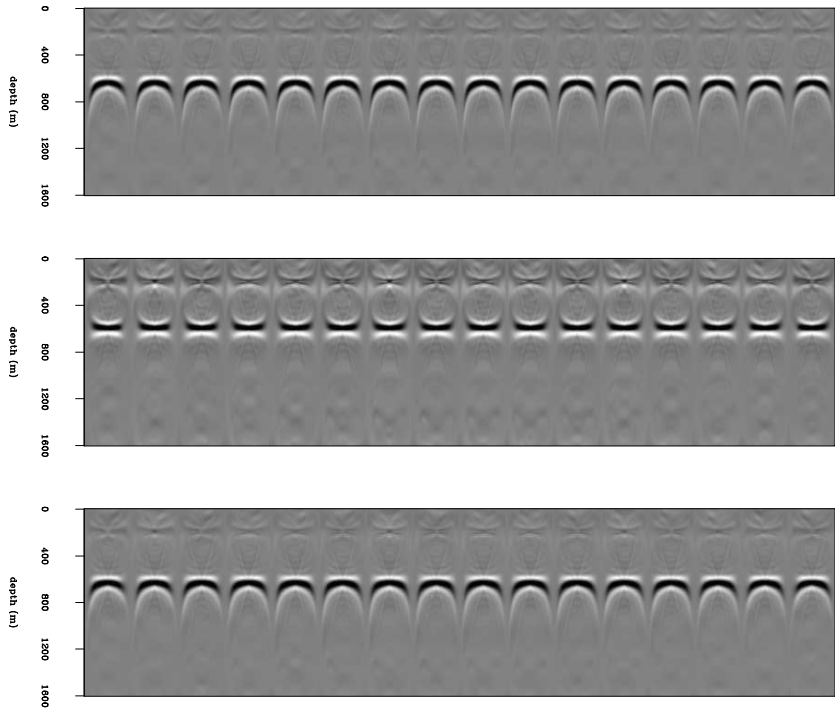

Figure 8: ADCIGs using the initial model in three cases. Top panel: Perturbation in velocity only; Middle panel: Perturbation in η only; Bottom panel: Perturbations in both. Curvature in the ADCIGs indicates errors in velocity or η. [**ER**]

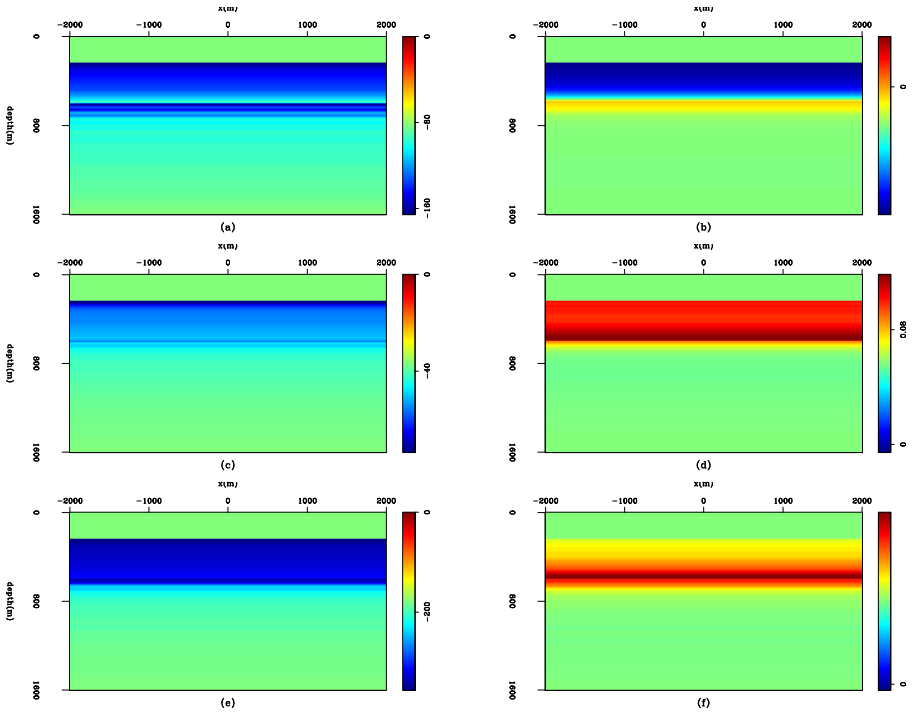

Figure 9: Inversion results of the three test cases. Panels are comparable to those in Figure 7. [**CR**]

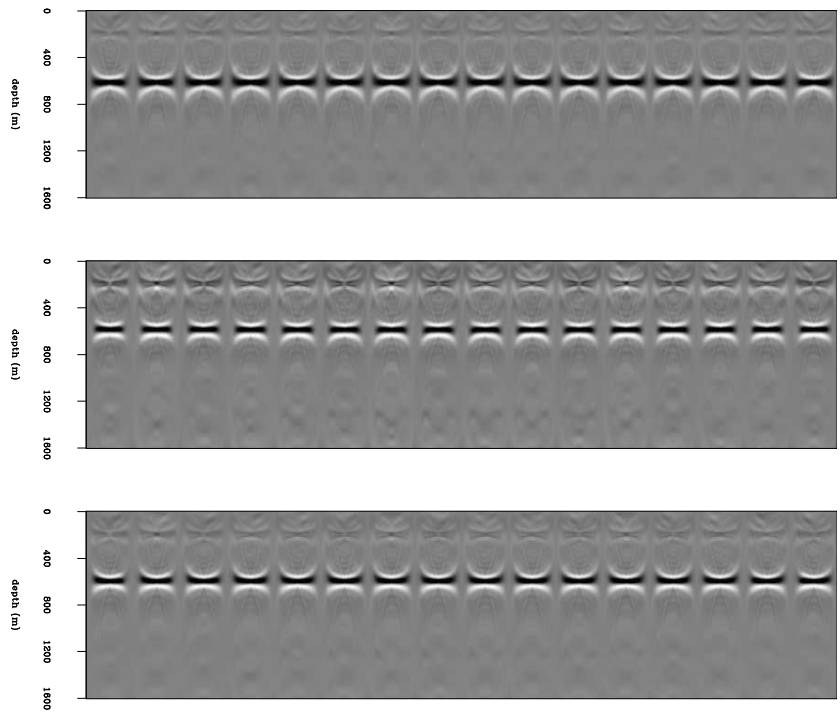

Figure 10: Common image gathers using the updated model in three cases. Top panel: Perturbation in velocity only; Middle panel: Perturbation in η only; Bottom panel: Perturbations in both. ADCIGs are flattened compared with Figure 8. [**ER**]

setting up the inversion problem with proper regularizations on proper data remains to be done. In order to accomplish this goal, I will focus my efforts on the following tasks:

Better parameterization of the model space. Current implementation uses the physical parameter - slowness and η; however, they have different units and magnitude in values. A better representation to balance these two model parameters is normalizing the slowness field with a characteristic slowness value (such as average). This is similar to the ray-based travel-time tomography, where phase velocity in different angle is normalized by the vertical P-wave velocity. Also the magnitude of gradient in these two parameter spaces are different by several orders as well. Experiment in the ray-based anisotropic tomography shows that after normalizing, the gradient in η (or ϵ) should be compansated by the corresponding slowness field (Zhou, personal contact). I will look into this and find the counterpart for the image-space wave-equation based method.

Better objective function. As described previously, the DSO objective function is easy to understand and implement, whereas its artifacts in the gradient and lack of ability to differentiate the illumination artifacts from model errors are not desirable. Therefore, a better objective function, such as WEMVA, could be a good substitution. Experiments on the isotropic velocity model building

show that WEMVA can provide a better defined image perturbation, which is consistent with Born approximation and thereby can be directly used to update the velocity model. Utilizing WEMVA as the objective function requires understanding of the residual migration for the anisotropic media, which is going to be my future research topic.

Adapt exploding-reflector modeling method. Current image-space wave-equation tomography carried out by the shot-profile migration engine requires a large amount of computation time, because it computes the SODCIGs on the entire grid and propagates one shot at a time. Application of exploding-reflector modeling will synthesize the data only in the area of interest, and the phase-encoded areal shots can be propagated at the same time without creating undesired cross-talks. Therefore, the computational cost could be reduced by order of magnitude. The generalization of the exploding-reflector modeling method for anisotropic media seems straightforward, nevertheless, the details during realization needed to be properly handled.

Experiment on different regularization schemes. Since the anisotropic model building introduces more parameters at each grid point, the problem is highly underdetermined. Therefore regularization plays a very important role in the inversion. In the previous sections, I discussed several potential regularizors that can be used to include the prior geological information. I plan to test the effects of different regularizor in different geological settings, and finally determine a general scheme for the proper application of each of them. I will also seek to collaborate with people working on interpretation (for example, the Rock Physics group) to incorporate as much as geological information as possible.

RESOURCES AND TIMELINE

Software

Most of the software needed is already available (at least for isotropic case) at SEP. Besides SEPlib and SEP3D, Madagascar is another source for multidimensional data analysis. I have coded the forward and adjoint image-space wave-equation tomography code as shown in the previous section. Tang and Clapp (2006) have developed a a method for selecting reference anisotropic parameters in laterally varying anisotropic media for mixed Fourier-space domain wavefield extrapolation, which can be used in 3-D anisotropic modeling and migration. Guerra and Biondi (2008) have designed a package to perform phase-encoded exploding-reflector modeling for the isotropic media, the generalization of which to anisotropic media should be straightforward. Clapp (2000) has developed a package to compute the 3-D steering filter based on the structure dip that can be used directly for regularization. Sava and Biondi (2004) have set up the complete theory and code for WEMVA in isotropic media, based upon

which I will develop its anisotropic counterpart. I have built up the preliminary inversion scheme for surface seismic data, and I will make corresponding changes when more data come available for my research.

Hardware

The proposed inversion scheme requires application of migration, forward and adjoint tomography several times in each iteration, and therefore it will take a large amount of computation time.

SEP currently has 6 shared memory machines, three with 16 nodes and 32 GB RAM shared memory and three with 8 nodes and 8 GB RAM shared memory. SEP also has 4 Linux clusters with a total of about 100 nodes. In addition, SEP students have access to CEES clusters and hard disks as well. Therefore, the computation resources are more than sufficient for my project.

Data

Synthetic model In SEP data library, there are at least two anisotropic synthetic datasets: Hess synthetic and Exxon synthetic. Anisotropic Hess model has a salt body, steep reflector (fault) and blocky anisotropic layers (Figure 11). Exxon synthetic has a salt body in the middle, and a smooth anisotropic field (Figure 12). These data are 2-D and relatively small, and thereby good test cases for my anisotropic model building algorithm in different settings.

Field data SEP data library already contains one field dataset from ExxonMobile that has shown anisotropic behavior. The anisotropic model estimated previously are shown in Figure 13. This dataset is 3-D, and has large lateral variations in the anisotropic parameters. Therefore, it could be a very good candidate to test my algorithm on real-world problem. In addtion, WesternGeoco has promised to SEP a field dataset with checkshots at several places, which fits to my idea of incorporating subsurface information. During my internship at WesternGeoco this summer, I will learn more about this dataset and tools to process and interpret the checkshots.

Timeline

- Ongoing: Test and optimize my current inversion code. I intend to finish testing my code on at least a small portion of the synthetic data mentioned in the previous section before the internship starts.

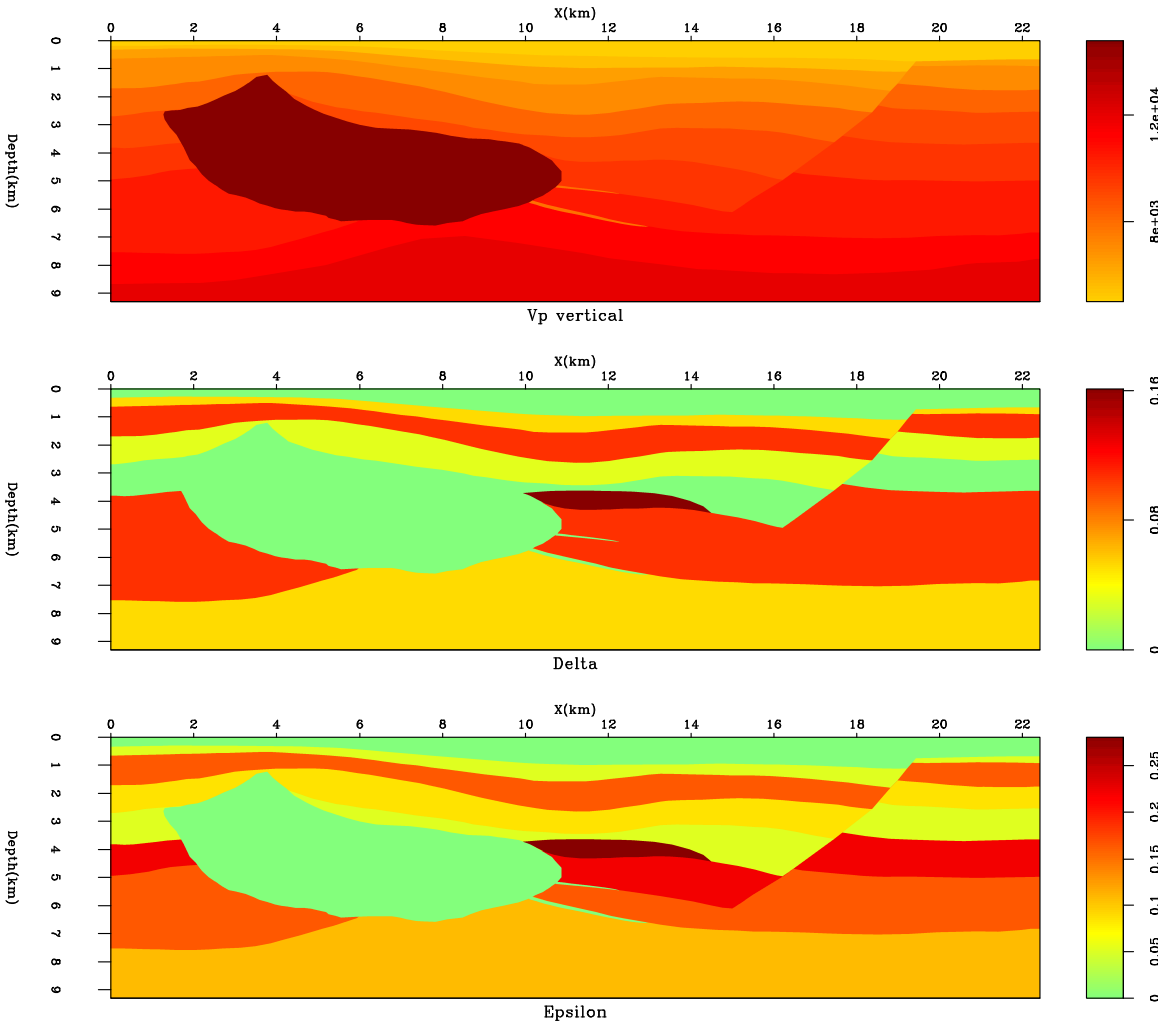

Figure 11: Anisotropic Hess model. Top panel: P-wave vertical velocity; Middel panel: Delta; Bottom panel: Epsilon.

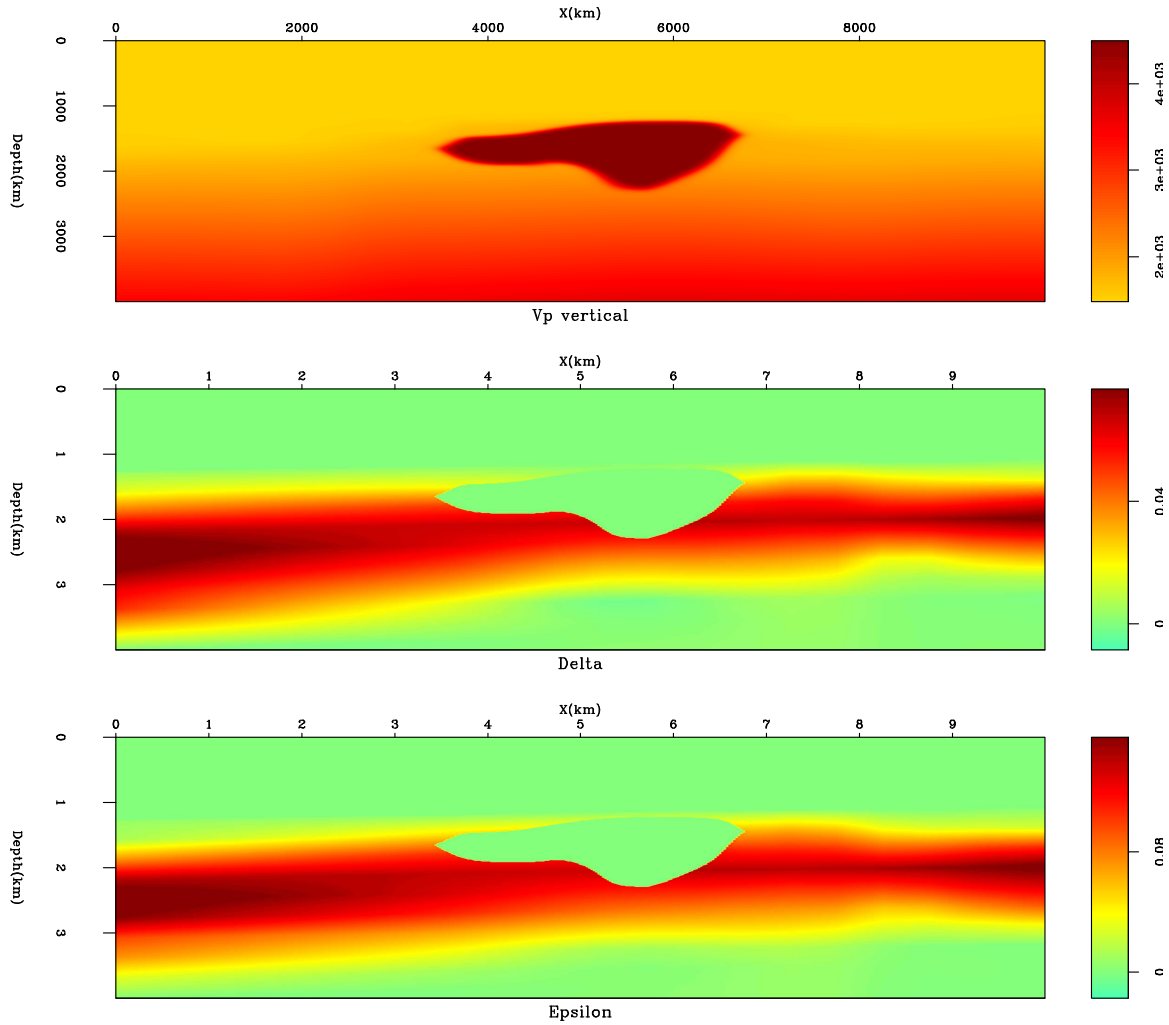

Figure 12: ExxonMobile synthetic model. Top panel: P-wave vertical velocity; Middel panel: Delta; Bottom panel: Epsilon.

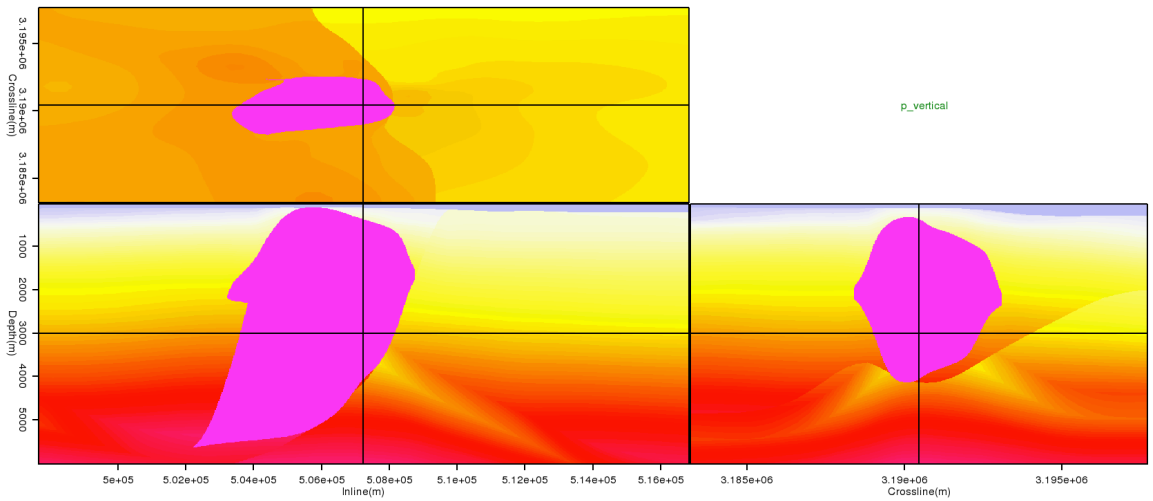

(a)

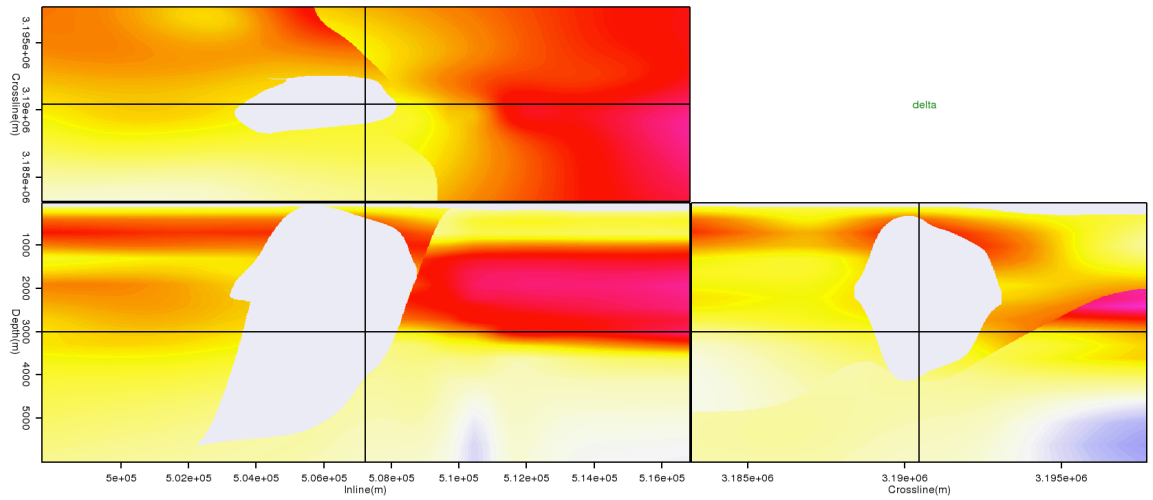

(b)

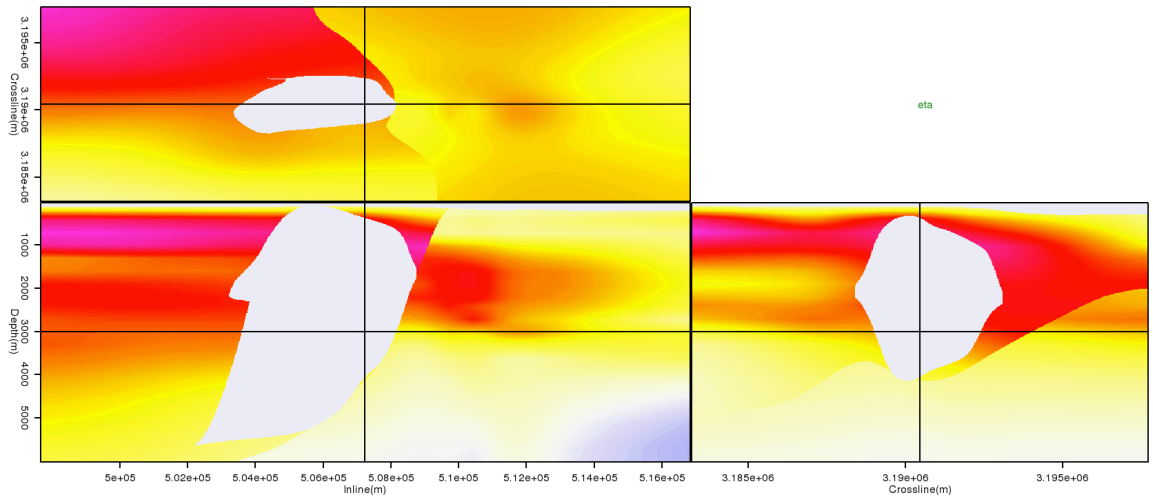

(c)

Figure 13: The anisotropic model estimated previously on the ExxonMobile field dataset. **(a)**: P-wave vertical velocity; **(b)**: Delta; **(c)**: Eta.

- Summer 2010: Internship at WesternGeoco. I hope to work on the dataset that will come to SEP, and gain experiences on how to process and interpret the field data and the checkshots.
- Fall 2010 - Winter 2010: Re-parameterize the model field, implement the code for different regularizors and test their response. Implement the phase-encoded exploding-reflector modeling for anisotropic media.
- Spring 2011 - Summer 2011: Generalize the idea of WEMVA to anisotropic case. Test the response of WEMVA gradient with respect to DSO gradient.
- Fall 2011 - Winter 2011: Optimize code, test on 2-D synthetic and field datasets.
- Spring 2012 - Summer 2012: Develop 3-D code, test on 3-D synthetic datasets
- Fall 2012 - Spring 2013: Test on 3-D field datasets.
- Summer 2013: Write thesis.
- Winter 2013: Graduate?

REFERENCES

Bakulin, A., M. Woodward, D. Nichols, K. Osypov, and O. Zdraveva, 2009, Building tti depth models using anisotropic tomography with well information: SEG Expanded Abstracts, **28**.

Biondi, B., 2006, Prestack exploding-reflectors modeling for migration velocity analysis: 76th Ann. Internat. Mtg., Expanded Abstracts, 3056–3060, Soc. of Expl. Geophys.

———, 2008, Automatic wave-equation migration velocity analysis: **SEP-134**, 65–78.

Claerbout, J. F., 1971, Towards a unified theory of reflector mapping: Geophysics, **36**, 467–481.

Clapp, R., 2000, Geologically constrained migration velocity analysis: PhD thesis, Stanford University.

Fei, T. W. and C. L. Liner, 2008, Hybrid fourier finite-difference 3d depth migration for anisotropic media: Geophysics, **73**, S27.

Fletcher, R., X. Du, and P. J. Fowler, 2009, Stabilizing acoustic reverse-time migration in tti media: SEG Expanded Abstracts, **28**.

Gallardo, L. A. and M. A. Meju, 2004, Joint two-dimensional DC resistivity and seismic travel time inversion with cross-gradients constraints: JOURNAL OF GEOPHYSICAL RESEARCH, **109**, doi:10.1029/2003JB002716.

Guerra, C. and B. Biondi, 2008, Prestack exploding reflector modeling: The crosstalk problem: **SEP-134**, 79–92.

Guerra, C., Y. Tang, and B. Biondi, 2009, Wave-equation tomography using image-space phase-encoded data: SEP-report, **138**, 95.

Kaarsberg, E., 1959, Introductory studies of natural and artificial argillaceous aggregates by sound-propagation and x-ray diffraction methods: J. Geol., **67**, 447–472.

McCollum, B. and F. Snell, 1932, Asymmetry of sound velocity in stratified formations: Physics (Journal of Applied Physics), **2**, 174–185.

Sava, P., 2004, Migration and velocity analysis by wavefield extrapolation: PhD thesis, Stanford University.

Sava, P. and B. Biondi, 2004, Wave-equation migration velocity analysis-I: Theory: Geophysical Prospecting, **52**, 593–606.

Shan, G., 2009, Optimized implicit finite-difference and fourier finite-difference migration for vti media: Geophysics, WCA189WCA197.

Shen, P., 2004, Wave-equation Migration Velocity Analysis by Differential Semblance Optimization: PhD thesis, Rice University.

Tang, Y. and R. G. Clapp, 2006, Selection of reference anisotropic parameters for wavefield extrapolation by lloyd's algorithm: **SEP-124**.

Zhang, Y. and H. Zhang, 2009, A stable tti reverse time migration and its implementation: SEG Expanded Abstracts, **28**.